

Blowing Iron Chalcogenides into Two-Dimensional Flaky Hybrids with Superior Cyclability and Rate Capability for Potassium Ion Batteries

Hu Wu,[†] Shiyao Lu,^{†,1} Siyuan Xu,[‡] Jing Zhao,[†] Yuankun Wang,[†] Chang Huang,[‡] Amr Abdelkader,[#] Wei (Alex) Wang,[∇] Kai Xi,^{,§} Yuzheng Guo,^{*,∗,‡} Shujiang Ding,^{*,†} Guoxin Gao,^{*,†} Ramachandran Vasant Kumar[○]*

[†]Xi'an Key Laboratory of Sustainable Energy Materials Chemistry, School of Chemistry, Xi'an Jiaotong University & Shaanxi Quantong Joint Research Institute of New Energy Vehicles Power, Xi'an Jiaotong University, Xi'an 710049, China.

[‡]Instrument Analysis Center, Electronic Materials Research Laboratory, Key Laboratory of the Ministry of Education & International Center for Dielectric Research, Xi'an Jiaotong University, Xi'an, Shaanxi 710049, China.

[§]Cambridge Graphene Centre, Department of Engineering, University of Cambridge, Cambridge CB3 0FA, United Kingdom.

¹Department of Chemistry, City University of Hong Kong, Hong Kong, China.

[‡]School of Electrical Engineering and Automation, Wuhan University, Wuhan 430072, China.

[#]Faculty of Science and Technology, Bournemouth University, Talbot Campus, Fern Barrow, Poole, BH12 5BB, United Kingdom.

[∇]Beijing Key Laboratory of Bio-inspired Energy Materials and Devices, School of Space and Environment, Beihang University, Beijing, 100191, China.

°Department of Materials Science and Metallurgy, University of Cambridge, Cambridge, CB3 0FS, United Kingdom.

*E-mail: gaoguoxin@mail.xjtu.edu.cn (G. Gao); kx210@cam.ac.uk (K. Xi); dingsj@xjtu.edu.cn (S. Ding); yguo@whu.edu.cn (Y. Guo).

ABSTRACT: Chalcogenide-based anodes are receiving increasing attention for rechargeable potassium-ion batteries (PIBs) due to their high theoretical capacities. However, they usually exhibit poor electrochemical performance due to poor structural stability, low conductivity and severe electrolyte decomposition on the reactive surface. Herein, a method analogue to “blowing bubbles with gum” is used to confine FeS₂ and FeSe₂ in N-doped carbon for PIBs anodes with ultrahigh cyclic stability and enhanced rate capability (over 5000 cycles at 2 A g⁻¹). Several theoretical and experimental methods are employed to understand the electrodes' performance. The density functional theory (DFT) calculations showed high affinity for potassium adsorption on the FeS₂ and FeSe₂. The *in-situ* XRD and *ex-situ* TEM analysis confirmed the formation of several intermediate phases of the general formula K_xFeS₂. These phases have high conductivity and large interlayer distance, which promote reversible potassium insertion and facilitate the charge transfer. Also, the calculated potassium diffusion coefficient during charge/discharge further proves the enhanced kinetics. Furthermore, The FeS₂@NC anode in a full cell also exhibits high cyclic stability (88 % capacity retention after 120 cycles with 99.9 % Coulombic efficiency). Therefore, this work not only provides an approach to overcome several challenges in PIBs anode but also a comprehensive understanding of the mechanism and kinetics of the potassium interaction with chalcogenides.

KEYWORDS: iron chalcogenide, fast ion transport, intermediate phases, “gel-blowing” strategy, potassium-ion batteries

Given the limitation and uneven distribution of lithium resources in the earth's crust (0.0017 wt%), the rapid growth of electric vehicles and renewable energy markets has stimulated the pursuit for efficient alternatives to commercial lithium-ion batteries (LIBs).¹ Benefiting from the abundant resource of Na (2.36 wt%) and K (2.09 wt%) in earth's crust, sodium-ion batteries (SIBs) and potassium-ion batteries (PIBs) have received increasing attention in the last few years.² Compared to SIBs, PIBs have the advantage of the lower standard electrode potential (-2.93 V for K^+/K vs -2.71 V for Na^+/Na), which guarantees a higher operating voltage and higher energy density for the batteries. In addition, among Li^+ , Na^+ and K^+ ions, potassium has the weakest Lewis acidity so that the *Stokes radius* of K^+ ion is the smallest in propylene carbonate (PC) solvents (K^+ (3.6 Å) < Na^+ (4.6 Å) < Li^+ (4.8 Å)).³ Hence, K^+ ion has the highest ion conductivity in organic electrolytes (~10 mS cm⁻¹ in 1 M PC) among these three alkali ions.^{3, 4} Especially, in PIBs, aluminium foil can be employed as the current collector because there is no alloying reaction with potassium, replacing the more expensive copper foil in LIBs (7200 \$ Mt⁻¹ for Cu vs 2100 \$ Mt⁻¹ for Al, the data were collected from <http://www.metal.com> on July 2020).

Despite the clear advantages of PIBs, several challenges need to be addressed before their commercial realization. High energy output needs electrodes that can sustain high energy densities and operate at high voltage windows.⁵ The larger K^+ means the volumetric changes are more significant in PIBs electrodes than other alkali metal batteries upon the repeated charging/discharging process, causing the fast structural collapse of the electrodes.^{6, 7} Hence, designing materials/electrodes that can maintain structural stability and ensure a long cycle life is another challenge. Also, the diffusivity of K^+ is significantly low in solid electrodes, constitute limitations on the reaction kinetics.⁸ Furthermore, PIBs suffers severe side reactions and

electrolyte decomposition on the electrodes due to the low electrochemical potential of K^+/K , which could allow the solvent in the electrolyte to be reduced.^{6,9} Several approaches have been employed in the literature to address some of the challenges mentioned above. For example, using intercalation-typed anodes, represented by carbonaceous and Ti-based materials,¹⁰⁻¹³ have been reported to deliver reasonable cyclability with low price. However, these intercalation-typed anodes often suffer from low capacities and poor rate capability because of their ordered structure with confined space for K^+ storage^{10, 14, 15}. Conversion-type (*e.g.*, MnO_2 ,¹⁶ MoS_2 ,¹⁷ and VSe_2 ¹⁸) and alloying-type anodes (*e.g.*, red P,¹⁹ Bi²⁰ and Sb²¹) could provide higher theoretical capacity. Nevertheless, their practical application in PIBs is hindered by the low conductivity and the large volume variation (*e.g.*, ~681% for Sn_4P_3) during cycling.⁴

Nanostructural design strategies have been employed to overcome some of the limitations of these anodes, including nanocrystallization,²² carbon-coating,²³ and hybridizing metal compounds with conductive matrixes (graphene,²⁴ MXene,¹⁴ *etc.*). The nanostructural design solutions allow developing advanced electrodes that use the synergy between robust structure and active materials with high theoretical capacity.²⁵ Amongst the reported active materials, transition metals oxides and chalcogenides have high theoretical capacities (usually >400 mAh g^{-1}). For instance, Fe-based materials (such as FeS_2) have been considered as one of the most promising electrode materials for LIBs, SIBs, and Li-S batteries because of their high theoretical capacity, low toxicity, and low cost (~ 400 \$ Mt^{-1} , the data were collected from <http://www.metal.com> on July 2020).²⁶⁻³⁸ Constrained by the intrinsic nature of the chalcogenides, it is difficult to obtain a robust nanostructure with fast ionic/electronic diffusion. While there is a clear need and probably a pathway to design more robust PIBs electrodes based on iron chalcogenides, several factors must be taken into consideration if one wants to go beyond incremental improvements. For instance, the design strategies should consider the surface physicochemical changes of the active

materials. By anionic substitution in the chalcogenides, the adsorption energy on the surface, the diffusion energy barrier and the interfacial reactivity can be regulated, which might boost the electrochemical performance.³⁹ More importantly, a deep understanding of the mechanism of interaction between K^+ and the active materials may promote designing electrodes that can simultaneously address most of the PIBs electrodes challenges.

Herein, we synthesized a series of Fe-based oxides and chalcogenide nanoparticles confined in nitrogen-doped carbon (denoted as $Fe_3O_4@NC$, $FeS_2@NC$ and $FeSe_2@NC$) nanosheets by a rapid “gel-blowing” strategy followed by a thermal conversion process. This hierarchical hybrid nanoarchitecture provides substantial active sites for potassium storage and shortens the electron/ion diffusion paths. The external carbon shell on the iron chalcogenide nanoparticles can suppress their aggregation and enhance the transfer kinetics. The potassium storage properties of Fe-based chalcogenides were investigated systematically by replacing of O, S and Se anions in the hybrid structure. Amongst the tested materials, $FeS_2@NC$ anode exhibits high reversible capacity (525.5 mAh g^{-1} at 0.1 A g^{-1}), record long-term cyclability (0.016% capacity loss per cycle over 5000 cycles) and excellent high-rate performance (154.7 mAh g^{-1} even at 10 A g^{-1}). The $FeS_2@NC$ electrode also exhibits excellent performance in full cell configuration with the considerable rate (230.4 mAh g^{-1} at a high rate of 2 A g^{-1}) and cycling stability (88 % capacity retention after 120 cycles). Additionally, through comprehensive *in-situ* and *ex-situ* characterization, combined with theoretical calculations, we explored the physicochemical properties of the hybrid electrodes. The results showed that the intermediate phases produced during charging and discharging are conducive and play a crucial role in the improvement of potassium storage of the original material. The results also showed that the interaction of K^+ with FeS_2 has low energy barriers, facilitating easier diffusion process and higher rate capacity; making $FeS_2@NC$ a promising anode material for PIBs.

RESULTS AND DISCUSSION

Figure 1a schematically illustrates the fabrication procedure of iron compounds (Fe_3O_4 , FeS_2 and FeSe_2) nanoparticles supported on 2D N-doped carbon (NC) nanosheets, which are denoted as $\text{Fe}_3\text{O}_4@\text{NC}$, $\text{FeS}_2@\text{NC}$ and $\text{FeSe}_2@\text{NC}$. For the fabrication of flaky $\text{Fe}_3\text{O}_4@\text{NC}$ samples, we employ a rapid “gel-blowing” strategy, which is quite analogous to “blowing bubbles with gum”.⁴⁰ First, Fe^{3+} ions are coordinated by the carboxylic groups of citric acid (CA) to form sol-gel coordination complex precursor. Second, this sol-gel precursor further reacts with ethylene glycol (EG) through the residual carboxylic groups in the CA to form a crosslinked viscous polyester gel. Then, the polyester gel is transferred into a tubular furnace to carry out the thermal “gel-blowing” treatment. Large volumes of pyrolysis gases (H_2O , CO_2 , *etc.*) are released to blow the viscous polyester gel into a large number of bubbles. These bubbles further expand and burst at high heating rates to form ultrathin NC nanosheets, which are decorated by ultrafine Fe_3O_4 nanoparticles, namely, $\text{Fe}_3\text{O}_4@\text{NC}$. For the fabrication of $\text{FeS}_2@\text{NC}$ and $\text{FeSe}_2@\text{NC}$ nanosheets, we employed thermal sulfuration and selenization processes respectively by heating $\text{Fe}_3\text{O}_4@\text{NC}$ with sulfur or selenium well above their melting point. As a result, Fe_3O_4 on the 2D NC is converted into sulfides or selenides, giving the conformal $\text{FeS}_2@\text{NC}$ and $\text{FeSe}_2@\text{NC}$ nanosheets.

The morphologies of the prepared composites are observed through the field-emission electron microscope (FESEM). **Figures 1b-g** reveal ultrathin sheet-like structure with micrometre-scale lateral dimension and decorated with fine particles for the three samples. **Figure 1c** demonstrates that the Fe_3O_4 nanoparticles (3-6 nm) are uniformly anchored onto the NC support, indicating that the uniform distribution of iron source in the polyester gel and the high-pressure insides the bubbles before their burst can prevent the aggregation and the extensive growth of Fe_3O_4 nanoparticles. As can be seen from **Figure 1d-g**, the flaky NC supports become thicker, and the sizes of FeS_2 and FeSe_2 particles on NC become slightly bigger after the

sulfuration or selenization conversion. The increase in the particle size could be attributed to the high exothermic reactions of the sulfuration and selenization processes, which led to rapid phase transformations and crystal growth of irregular FeS₂ and FeSe₂ particles. The SEM images of FeS₂@NC show that FeS₂ particles are relatively evenly distributed on the NC matrix (Figure S1, see Supporting Information). Interestingly, the TEM images distinctly show that there is a thin amorphous carbon layer on the surface of fine FeS₂ and FeSe₂ nanoparticles (insets of Figure 1e, 1g). This amorphous carbon coating is beneficial in improving the electrochemical performance of the composites, as will be discussed later.

The crystalline structure and phase purity of the as-prepared Fe₃O₄@NC, FeS₂@NC and FeSe₂@NC are determined by X-ray diffraction (XRD). As shown in Figure 2a, all the dominant diffraction peaks of the three samples are well indexed to the magnetite Fe₃O₄ phase (JCPDS no. 19-0629), pyrite FeS₂ phase (JCPDS no. 42-1340) or ferroselite FeSe₂ phase (JCPDS no. 82-0269), respectively, confirming the successful fabrication of these composites. No diffraction peaks from any impurities are detected, implying the high purity of the prepared Fe-based@NC composites. The surface elemental compositions of as-prepared composites are measured by energy dispersive X-ray (EDX) spectroscopy, as displayed in Figure S2 (see Supporting Information). As-expected, nitrogen elements can be detected in all three samples, meaning the carbon sheets are doped by nitrogen elements from iron nitrate and ammonia in the reactant. The Raman spectra (Figure 2b) showed two distinctive broad peaks at 1332 cm⁻¹ (D band) and at 1582 cm⁻¹ (G band), confirming the existence of carbonaceous component in the three samples. The peak intensity ratio (I_D/I_G) is almost the same for the three samples, implying that the carbon matrix in the composites has a similar structure. The carbon contents of Fe₃O₄@NC, FeS₂@NC and FeSe₂@NC, determined by thermogravimetric analysis (TGA), are about 45.3 wt%, 29.1 wt% and 26.4 wt% (Figure 2c), respectively. To obtain more details about the oxidation state and

the bonding between the constituents in the Fe₃O₄@NC, FeS₂@NC and FeSe₂@NC composites, the X-ray photoelectron spectroscopy (XPS) was performed. As shown in **Figure S3** (see Supporting Information), six main elements of Fe, S (O, Se), C and N are detected clearly on the survey spectra of corresponding three samples. The elemental compositions are listed in **Table S1** (see Supporting Information). **Figure 2d-f** show the high-resolution Fe 2p, S 2p and N 1s XPS spectra of the FeS₂@NC sample. In the Fe 2p spectrum, two spin-orbital splitting peaks observed at 720.2 and 707.4 eV can be ascribed to Fe 2p_{1/2} and Fe 2p_{3/2}. The broad peak at 710.9 eV is derived from the Fe³⁺ state and can be attributed to the surface oxidation of FeS₂ nanoparticles. The small peak at 708.4 eV may originate from the electron-deficient sites caused by the breaking of the Fe-S bonds.⁴¹ In the high-resolution S 2p spectrum (**Figure 2e**), five peaks can be detected at 162.7, 163.9, 164.3, 165.6 and 168.7 eV, and are attributed to the S 2p_{3/2} (FeS₂), S 2p_{1/2} (FeS₂), S 2p_{3/2} (C-S), S 2p_{1/2} (C-S) and C-SO_x-C, respectively.^{42, 43} The presence of several oxidation states of S in the C-S bond suggested S is connected to C in more than one form; the in-plane doping of the 2D NC; and an off-plane link between NC and FeS₂ nanoparticles. When carefully compared with the S 2p spectrum of a controlled N and S co-doped carbon (SNC) sample, a right shift of C-S (S 2p) thiophene-S peak can be observed (**Figure 2e**). This shift can be attributed to the electron donating Fe atoms, suggesting that FeS₂ particles and the NC matrix may have chemical bonds. We further proved the bond between C and S by comparing the FTIR spectra of FeS₂@NC with the controlled SNC sample. As shown in **Figure 2d**, the stretching vibration peak of the C-S bond in FeS₂@NC was shifted from 668 to 656 cm⁻¹ due to the inductive effect of Fe on the C-S bond. Further, the fitted peak of C-S bond is also appeared at 285.5 eV on C 1s spectrum of FeS₂@NC, but not on the Fe₃O₄@NC spectrum (**Figure S4b** and **Figure S5c**, see Supporting Information). These results confirm the formation of FeS₂ and also suggest a strong bond between the NC nanosheets and the sulfide nanoparticles. The high-resolution N 1s

spectrum shown in **Figure 2f** delivers three well-defined characteristic peaks at 401.1, 399.6 and 398.6 eV, corresponding to the pyridinic-N, pyrrolic-N and graphitic-N, respectively. The pyridinic-N and pyrrolic-N can induce numerous defects and create more active sites, thus benefiting the potassium storage performance of as-prepared FeS₂@NC electrodes.⁴⁴ The C 1s spectrum (**Figure S4**, see Supporting Information) can be divided into three peaks, pointing to C-C/C=C, C-S, C-N and O=C-O bonds, also confirming the successful doping of carbon nanosheets with nitrogen element.^{45, 46} Meanwhile, the high-resolution XPS spectra of Fe 2p, O 1s, C 1s and N 1s for Fe₃O₄@NC sample (**Figure S5**, see Supporting Information) and Fe 2p, Se 3d, C 1s and N 1s for FeSe₂@NC sample (**Figure S6**, see Supporting Information) both confirm the as-anticipated hierarchical hybrid structure. It should be mentioned here that the presence of O elements in FeS₂@NC and FeSe₂@NC is probably due to the partial surface oxidation and air adsorption of the tested samples upon carrying out the XPS measurements.

The hierarchical hybrid structures are further investigated by transmission electron microscopy (TEM). As shown in **Figure 3a-c**, all the fine iron oxide or chalcogenide particles are uniformly distributed on the surface of NC nanosheets without apparent aggregation. The selected area electron diffraction (SAED) patterns (**insets of Figure 3a-c**) reveal well-defined diffraction rings, revealing the polycrystallinity feature of all three composites. The smooth electron diffractions of Fe₃O₄@NC sample imply that the crystalline Fe₃O₄ nanoparticles have small grain size (3-6 nm) with random orientations. The bright diffraction spots are observed in the SAED patterns of FeS₂@NC and FeSe₂@NC, further confirming the excellent crystallinity of FeS₂ and FeSe₂ particles growing on NC substrates. The high-resolution TEM (HRTEM) images demonstrate the (311) and (220) crystal planes of magnetite Fe₃O₄ (**Figure 3d**), the (211) crystal plane of pyrite FeS₂ (**Figure 3e**), and the (110) and (011) crystal planes of ferroselite FeSe₂ (**Figure 3f**). Elemental mapping analysis (**Figure 3g-i**) shows uniform distribution of N in the

NC nanosheets. In addition, Fe and O (S, Se) elements in the designed structures overlap very well with the area where the nanoparticles are located, further confirming the successful phase conversion of Fe₃O₄ into FeS₂ and FeSe₂.

We then investigated the electrochemical performance of the prepared iron-based composites as electrodes for potassium ion batteries *via* assembling coin-type half-cells. **Figure 4a-b** and **S6a-c** (see Supporting Information) demonstrate the charge-discharge profiles of Fe₃O₄@NC, FeS₂@NC and FeSe₂@NC electrodes at a current density of 0.5 A g⁻¹. Unlike Fe₃O₄@NC anode, both FeS₂@NC and FeSe₂@NC anodes showed similar charge-discharge curves, suggesting similar electrochemical reaction mechanism. In the initial discharge process, both FeS₂@NC and FeSe₂@NC anodes deliver a distinguished voltage plateau at ~1.1V. This voltage plateau disappears quickly after the first charge-discharge cycle, which is in a good agreement with most reported transition metal chalcogenide-based anodes for PIBs.^{15, 31, 35, 47} To clarify the potassium storage mechanism, we further carried out cyclic voltammetry (CV) measurements for each composite anode at a scan rate of 0.5 mV s⁻¹. As shown in **Figure S8a-c** (see Supporting Information), the CV curves of Fe₃O₄@NC anodes are also different from that of FeS₂@NC and FeSe₂@NC anodes in the first five cycles, implying a different potassium storage mechanism. The irreversible peak in the initial cathodic scan can be ascribed to the formation of solid electrolyte interphase (SEI), side reactions and the potassium intercalation process.⁴⁷ Still, no obvious peaks can be detected during the subsequent cycles, suggesting limited K storage capability. The dichalcogenides electrodes, FeS₂@NC and FeSe₂@NC, display more pronounced irreversible reduction peaks in the initial cathodic scan, indicating more active electrode surface. In the anodic scan, the CV curves almost coincide during the first five cycles, especially for the FeS₂@NC anode, suggesting high electrochemical reversibility.

Figure 4c and **S6d-f** (see Supporting Information) present the cycling performance and

Coulombic efficiency of the anodes at 0.5 A g⁻¹. All Fe-based anodes demonstrate good cyclic stability in the short-range at low current density. Nonetheless, Fe₃O₄@NC anode delivers the lowest reversible capacity of 140.6 mAh g⁻¹ while FeS₂@NC anode provides the highest capacity of 413.7 mAh g⁻¹ after 100 cycles. **Figure 4d** compares the rate performances of Fe₃O₄@NC, FeS₂@NC and FeSe₂@NC anodes. Both FeS₂@NC and FeSe₂@NC anodes have much better rate performance than Fe₃O₄@NC anode, which might be attributed to the low reactivity with K⁺ ions and the poor electronic conductivity of pure Fe₃O₄. On the other hand, as the optimal potassium storage materials, FeS₂@NC anode shows high-rate capability with the reversible specific capacities of 236.1 mAh g⁻¹ at 5.0 A g⁻¹ and 154.7 mAh g⁻¹ at 10.0 A g⁻¹. More interestingly, once the current densities come back to 1.0 A g⁻¹ and then 0.5 A g⁻¹ for another 10 cycles, the specific capacities of the FeS₂@NC electrode quickly recover to 348.7 and 404.2 mAh g⁻¹, respectively, indicating high reversibility after the high-rate cycling. The high-rate performance of the FeS₂@NC anodes presented in the current work outperformed other reported electrodes, including most transition metal dichalcogenides/oxides and carbon-based materials,^{6, 10, 15, 18, 21, 24, 31-33, 48-58} as illustrated in **Figure 4e**. The FeSe₂@NC anode also exhibits excellent rate performance with slightly lower reversible capacity (133.2 mAh g⁻¹ at 10.0 A g⁻¹) than FeS₂@NC anode. **Figure 4g** further compares the long-term cycle stabilities of three kind iron-based composite anodes cycled at 2 A g⁻¹. Notably, even after 5000 cycles, the FeS₂@NC anode can still deliver a stable discharge capacity of about 73.6 mAh g⁻¹, which is almost three-time higher than that of the FeSe₂@NC (24.1 mAh g⁻¹). The capacity attenuation for FeS₂@NC electrode is only 0.016 % per cycle with ~100 % Coulombic efficiency over the 5000 cycles, reflecting the superiority over other reported materials (**Figure 4f**).^{6, 15, 18, 19, 21, 24, 31, 33, 35, 48-50, 52, 53, 55, 59-61}

The Fe₃O₄@NC anode, on the other hand, suffers from rapid capacity fade upon the cycling

at the same current density with the discharge capacity sharply drops to 39.2 mAh g⁻¹ after only 200 cycles. In order to disclose the capacity contribution of NC matrix in the hybrid composites, we etched Fe₃O₄@NC powder in 4 M HCl solution under slightly magnetic stirring for 24 h to obtain pure NC sheets. The electrochemical results are shown in **Figure S9** (see Supporting Information). It can be seen that the pure NC sheets can deliver a reversible capacity of about 155.6 mAh g⁻¹ after 100 cycles at 0.5 A g⁻¹, higher than that of Fe₃O₄@NC (140.6 mAh g⁻¹), further confirming that Fe₃O₄@NC composites are not suitable as anode materials for PIBs. Therefore, in the subsequent investigation, we will focus on the potassium storage mechanism of FeS₂@NC and FeSe₂@NC mainly.

Density functional theory (DFT) calculations were employed to further investigate the electrochemical behaviour and physicochemical properties of the FeS₂@NC and FeSe₂@NC anodes. As displayed in **Figure S10** (see Supporting Information), the calculated density of states (DOS) show that the FeSe₂ (001) surface had a smaller bandgap (0.16 eV) compared with FeSe₂ (110) and FeS₂ (001) surfaces (0.92 and 0.53 eV, respectively). The low bandgap implying that the electron movement is easier in the (001) direction, and FeSe₂ has high electronic conductivity. Based on the adsorption energy calculation, **Figure 5a-c**, the adsorption energy values of K are negative at all selected sites on FeS₂ and FeSe₂ surfaces, suggesting spontaneous adsorption. The affinity of the FeS₂ surface to adsorb K is higher than that of FeSe₂, judging by the more negative adsorption energy. Furthermore, on both materials, all sites yield more or less the same energy values, demonstrating that the atoms can move to the same place during the relaxation. After examining the final optimized image, this place turned out to be site1 for both materials, which is considered as the best adsorption position. Consequently, site1 was chosen as the initial and final position in the diffusion process. In the diffusion process (**Figure 5d**), the combination of K and FeS₂ showed a relatively lower energy barrier (59.42 meV for FeS₂ vs 194.72 meV for FeSe₂),

indicating an easier diffusion process and higher rate capacity when applied to batteries. It is interesting to find that although share a similar structure, the easiest diffusion path on FeS₂ (001) was not convergent on FeSe₂ (110) during the calculation. We inferred that is because the larger radius of Se atom blocked this path. It can be concluded from these calculations that the designed FeS₂@NC and FeSe₂@NC have the excellent advantages of promoting stronger chemical adsorption with K⁺ and enhancing the charge-transfer kinetic within the electrode.

To disclose the changes in structure and morphology upon cycling, we carried out *ex-situ* FESEM and TEM observation on FeS₂@NC and FeSe₂@NC electrodes after 50 cycles at 0.5 A g⁻¹. As shown in **Figure S11** (see Supporting Information), the *ex-situ* FESEM images display that the morphology of the FeS₂@NC electrode hardly changes in the micro-scale except for a slight thickness increase of NC support. The *ex-situ* TEM images (**Figure S12**, see Supporting Information) reveals slight volume expansion after being discharged to 0.01 V and then charged to 2.5 V again, thus demonstrating excellent cycle stability of the FeS₂@NC electrode. On the other hand, some particles on FeSe₂@NC have peeled off the electrode after cycling, which is responsible for the capacity loss of FeSe₂@NC electrodes. The electrochemical impedance spectroscopy (EIS) analysis for FeS₂@NC and FeSe₂@NC, **Figure S13** (see Supporting Information), agrees with the FESEM, TEM, DTF calculation and the electrochemical charge/discharge results. From the EIS plots, we can find that the diameter of the semicircle (charge transfer resistance (R_{ct})) of the electrodes at high-frequency field reduces sharply after being activated for 30 cycles, indicating rapid enhancement of their ionic/electronic conductivity upon a moderate activation process. The FeS₂@NC anode demonstrates the smallest semicircle at high frequency (R_{ct} = 850 Ω), indicating the highest ionic/electronic conductivity of the studied electrodes.

As well known, the potential pseudocapacitive behavior of electrode materials has been

considered as an advantageous factor for their high-rate performance upon continuous charge-discharge cycling. Therefore, the capacitive contribution of the Fe-based electrodes was determined by investigating the CV curves at various scan rates (0.2 ~ 1.0 mV s⁻¹) in the voltage window of 0.01-2.5 V to shed more light on the electrochemical reaction kinetics (**Figure 6a-c**). Generally speaking, on the CV profiles, the redox peak current (*i*) and the scan rate (*v*) follow the equation:^{62, 63}

$$\log(i) = b\log(v) + \log a \quad (1)$$

where *a* and *b* are adjustable parameters, and *b*-value can be read from the slope of the log(*i*) vs log(*v*) plots. The electrochemical process is considered to be mainly controlled by the ionic diffusion when the value of *b* is about 0.5, while dominated by the capacitance behavior if *b*-value approaches to 1.0. As shown in **Figure S14** (see Supporting Information), the *b*-values (fitted slopes) of Fe₃O₄@NC anode are 0.73 and 0.71, implying the ionic diffusion behavior plays an important role on controlling the electrochemical process. On the contrary, the *b*-values of FeS₂@NC and FeSe₂@NC are all close to 1.0, meaning the pseudocapacitive behavior originating from fast surface redox reaction dominates the electrochemical process. Specifically, the total pseudocapacitive contribution can be calculated through the following equation: $i = k_1v + k_2v^{1/2}$, where k_1v and $k_2v^{1/2}$ represent the pseudocapacitive and ionic diffusion contributions, respectively.^{62, 63} As shown in **Figure 6d**, the electrochemical potassium storage process of the Fe₃O₄@NC electrode is controlled by the ionic diffusion and the contribution fractions are all above 50% at different scan rates ranging from 0.2 to 1.0 mV s⁻¹, which leads to the sluggish electrochemical reaction between K⁺ and Fe₃O₄ particles and presents inferior rate capability. On the other hand, FeS₂@NC and FeSe₂@NC electrodes exhibit higher pseudocapacitive contributions (over 60%) as can be seen from **Figure 6e-f**. Especially at a high scan rate of 1.0 mV s⁻¹ (**Figure S15**, see Supporting Information), the pseudocapacitive contributions of

FeS₂@NC and FeSe₂@NC reach 77.8% and 77.2%, respectively. This strongly confirms the potassium storage reactions of the chalcogenide anodes are both dominated by the pseudocapacitive behavior, delivering excellent high-rate performance.

To further investigate the electrochemical reaction kinetics, the potassium ion diffusion coefficient (D_{K^+}) was calculated using the galvanostatic intermittent titration technique (GITT). The tested electrodes were activated at 0.5 A g⁻¹ for five cycles to form a stable SEI film before carrying out the GITT measurement. The D_{K^+} was calculated according to equation 2:^{47, 64, 65}

$$D_{K^+} = \frac{4}{\pi\tau} \left(\frac{m_B V_M}{M_B A} \right)^2 \left(\frac{\Delta E_s}{\Delta E_\tau} \right)^2 \quad (2)$$

where, τ is the time of the pulse current (herein, $\tau = 900$ s), m_B is the mass of electroactive materials on the current collector, M_B and V_M are the molar mass and molar volume of electroactive material, respectively, A is the surface area of the tested electrode, ΔE_s is the steady-state potential difference before and after the application of current pulse, and ΔE_τ is the instantaneous potential difference at the beginning and end of the current pulse (**Figure S16**, see Supporting Information). To further simplify the calculations, Equation 2 can be approximated as follows:⁶⁴

$$D_{K^+} = \frac{4}{\pi\tau} L^2 \left(\frac{\Delta E_s}{\Delta E_\tau} \right)^2 \quad (3)$$

where, L refers to the diffusion length of K⁺ ions, which can be replaced by the thickness of the electrode material. **Figures 6g-i** reveal the GITT curves and the corresponding diffusion coefficient of K⁺ in Fe₃O₄@NC, FeS₂@NC and FeSe₂@NC anodes as a function of the reaction depth. The discharge and charge profile of Fe₃O₄@NC shows more significant fluctuation, indicating its high overpotential caused by the slow process kinetics. The fast diffusion of K⁺ in the FeS₂@NC electrode is clearly evidenced by the moderate D_{K^+} during the potassiation process and the high D_{K^+} when depotassiation.

Usually, transition-metal dichalcogenides exhibit quite complicated conversion reaction mechanisms in metal-ion batteries. To reveal more detailed information of the reaction mechanism on the FeS₂@NC electrodes, *in-situ* XRD and *ex-situ* TEM was employed. For the *in-situ* XRD observation, we assembled a customized cell, as illustrated in **Figure S17** (see Supporting Information). **Figure 7a** shows the first voltage-discharge curve on the left and the *in-situ* XRD contour plots of FeS₂@NC electrode on the right side. The peak at 38.7° with constant intensity is derived from the Be window. The results show that potassium storage has a stepwise feature. During the discharge process, the intensity of the peaks at 33.0°, 37.1° and 40.8°, corresponding to the (220), (210) and (211) crystal planes of pyrite FeS₂ respectively, fades gradually until disappearing at 0.2 V, indicating that FeS₂ has fully reacted. The reflections at 30.9°, 31.4° and 35.9° are always observed in the charging process, which can be indexed to the K⁺ inserted phases of the general formula K_xFeS₂. Interestingly, K_xFeS₂ can still be maintained when charging to 2.5V. The selected *in-situ* XRD patterns with 2θ ranging from 31.5° to 34.5° are shown in **Figure 7b**. It can be seen that the FeS₂ (200) peak reappears with increasing of voltage during charging, indicating that the electrochemical reaction of FeS₂ is partially reversible. Further evidence is given by the *ex-situ* HRTEM images and the corresponding SAED patterns of the products after being discharged to 0.01 V and then charged to 2.5 V. The HRTEM image at fully discharged state (0.01 V, **Figure 7c**) displays legible lattice fringes with the interplanar distances of 0.594 nm and 0.583 nm, matching well with the (101) and (002) crystal planes of K₃(FeS₂)₂, respectively. The corresponding SAED patterns (**Figure 7d**) also show that the d-spacings of the diffraction rings can be assigned to the (132), (124) and (144) planes of K₃(FeS₂)₂. These results demonstrate that the reflection in the dotted red circle (**Figure 7a**) corresponds to the (221) plane of K₃(FeS₂)₂ phase. The (111) and (200) plane of metallic Fe can also be observed in these SAED patterns, implying that K₃(FeS₂)₂ is partially transformed into Fe

and K_2S when discharged to 0.01V (**Figure S18a**, see Supporting Information). **Figure 7e** and **7f** further confirm that the fully charged products are FeS_2 and $KFeS_2$ since the detected lattice spacings are well indexed to FeS_2 and $KFeS_2$. Therefore, it can be concluded that the phase evolution process of $FeS_2@NC$ is not consistent with the prediction of a typical conversion reaction mechanism. Similarly, neither $Fe_3O_4@NC$ nor $FeSe_2@NC$ can undergo a complete conversion reaction (**Figure S19-20**, see Supporting Information). According to the reversible equation: $FeS_2 + 4K^+ + 4e^- \rightarrow Fe + 2K_2S$, and the formation of intermediate K_xFeS_2 phase,^{30, 31, 35, 61} the theoretical specific capacity of FeS_2 can reach 893 mAh g^{-1} . Although the incomplete conversion reaction can cause capacity loss, the larger lattice spacing of intermediate K_xFeS_2 is favorable for the re-insertion of K^+ ions upon cycling (**Figure S18b**). In addition, K_xFeS_2 is a conductive phase (0 eV bandgap⁶⁶) and can compensate for the poor conductivity of FeS_2 at the fully charged state. Therefore, we believe that the intermediate K_xFeS_2 phase is responsible, at least partially, for improving the high cyclic stability and rate performance of the $FeS_2@NC$ electrodes.

Next, we investigated two intermediate phases (K_xFeS_2 , $x=1, 1.5$) containing different quantities of K atoms, and also calculated the adsorption energy of K on the (001) surface of these two structures. Furthermore, we examined the adsorption energy of these two phases coated with a graphene layer. As shown in **Figure 7g-j**, two different positions were chosen to calculate the adsorption energy of the K atom. The results are shown in **Table 1**. The negative adsorption energy demonstrates that K atom could be well adsorbed on both two sites. The results also show that the adsorption energy is higher when a layer of graphene is on the top of $K_3(FeS_2)_2$ (001) surface. Since site2 shows a better affinity to K (the most negative adsorption energy -3.78 eV), the top of the central S atom is considered to be the favorite adsorption site. **On the $KFeS_2$ (001) surface, we chose three different sites owing to its less symmetric structure compared with the**

previous surface, as shown in **Figure 7k-n**, which locate above the Fe, S, K atom, respectively. All the selected sites exhibit negative energy with almost equal values, suggesting that K atoms can move to site3 during the relaxation, which was proved the most stable adsorption location. Similar to the $K_3(FeS_2)_2$, the adsorption of K on $KFeS_2$ (001) significantly improves when adding a layer of graphene with energy value reaching about -3.06 eV. The adsorption energy of K on both $K_3(FeS_2)_2$ and $KFeS_2$ is more negative than the one calculated for the FeS_2 electrode (**Figure 5c**), in line with the *in-situ* XRD and *ex-situ* TEM conclusion that K_xFeS_2 is responsible for improving the electrode performance. It should be mentioned here that, the DFT calculation has provided an explanation for the poor electrochemical performance of the $Fe_3O_4@NC$ hybrid, and hence we limited our discussion on sulfides. More details and discussion on the $Fe_3O_4@NC$ electrode performance are in the supporting information (Figure S21 and the relevant discussion)

In the electrochemical test, the loading of the active material per unit area of the electrode is an important factor in determining the overall performance and the visibility of scaling up. All the results mentioned above used a loading of the active material ranged between 1.0-1.5 mg cm⁻², which is relatively high loading when compared with published work (**Table S2**, see Supporting Information). To verify the potential application of the $FeS_2@NC$ anode in PIBs, we further tried higher mass loading of 2.0 and 2.5 mg cm⁻². As shown in **Figure S22**, the cells with high loading maintain good cyclic stability with a negligible capacity loss after 100 cycles.

In order to be closer to practical applications, we have tested the $FeS_2@NC$ anode in a full-cell configuration using a composite of polyimide and reduced graphene oxide (denoted as PI@rGO) as the cathode (**Figure 8a**). The charge and discharge curves of $FeS_2@NC // K$ half-cell, $FeS_2@NC // PI@rGO$ full cell and $PI@rGO // K$ half-cell are shown in **Figure 8c**. The working voltage of the full cell is around 1.6 V, which is between that of $FeS_2@NC // K$ and $PI@rGO // K$ cells. It can be seen from **Figure 8d** that the charge and discharge plateaus of the

full cell preserved with slight polarization when the current density increased from 0.1 to 2 A g⁻¹, suggesting excellent rate performance. **Figure 8e** displays the corresponding rate and cycling performance. As the current density increases from 0.1 to 0.2, 0.5 1.0 and 2.0 A g⁻¹, the full cell shows reversible capacities of 260, 252, 246, 239 and 230 mAh g⁻¹, respectively. When the current density comes back to 0.5 A g⁻¹, the specific capacity quickly recovered to 241 mAh g⁻¹. Even after 120 cycles at 0.5 A g⁻¹, there is still a reversible capacity of 228 mAh g⁻¹ representing 88 % capacity retention. Interestingly, the Coulomb efficiency after the cell is stabilized as high as 99.9%, and the average capacity attenuation per cycle is only 0.149 mAh g⁻¹ at 0.5 A g⁻¹ within the 120 cycles. Therefore, the FeS₂@NC is a promising anode material for potassium storage in practical applications.

CONCLUSIONS

In this research, hierarchical hybrid structures of Fe-based chalcogenide nanoparticles anchored on nitrogen-doped carbon flake (Fe₃O₄@NC, FeS₂@NC and FeSe₂@NC) were developed by a facile and scalable strategy. In such structures, the ion/electron transfer efficiency is significantly enhanced, and the electrochemical process controlled by the surface redox reaction promotes rapid charge transfer, resulting in excellent rate performance and long cycle stability for PIBs. Notably, the as-prepared FeS₂@NC sample displays the high reversible capacity of 525.5 mAh g⁻¹ at 0.1 A g⁻¹, superb rate performance of 154.7 mAh g⁻¹ even at 10 A g⁻¹ and excellent long-term cyclability over 5000 cycles. **The FeS₂@NC anode was also tested in a full cell configuration, and the cell exhibits high capacity retention of 88 % after 120 cycles with promising Coulombic efficiency of 99.9 %.** The DFT calculations showed that the surface of FeS₂ has higher adsorption energy and lower ion diffusion barrier compared with FeSe₂.

Meanwhile, the $K_x\text{FeS}_2$ intermediate phases observed in the experiment exhibit more negative adsorption energy, and the carbon composition in the hybrid structure, including externally coated carbon layer and the 2D NC matrix, further promote the adsorption capacity of the electrode material to K. The material design ideas presented in our work provide an opportunity to develop practical high-performance electrode materials for battery systems.

METHODS

Synthesis of $\text{Fe}_3\text{O}_4@\text{NC}$. The $\text{Fe}_3\text{O}_4@\text{NC}$ was synthesized by a rapid “gel-blowing” strategy. In a typical experiment, 6.0 g of $\text{Fe}(\text{NO}_3)_3 \cdot 9\text{H}_2\text{O}$ and 6.0 g of citric acid were dissolved into 6.5 mL deionized water. Then, 6.0 mL of ethylene glycol was added to the solution, and the mixture was vigorously stirred. The pH value was maintained at 7 using ammonium hydroxide. The dark green solution was then heated at 100 °C for 10 h in an oil bath. The resulting gel was transferred to a tube furnace and heated for at a temperature of 500 °C under continuous flow of Ar gas. After cooling to room temperature, a fluffy black product was obtained.

Synthesis of $\text{FeS}_2@\text{NC}$ and $\text{FeSe}_2@\text{NC}$. The as-prepared $\text{Fe}_3\text{O}_4@\text{NC}$ was mixed with sulfur powder in a mass ratio of 1:3. The mixture was then charged into a quartz tube and annealed at 400 °C for 4 h under argon to obtain the desired $\text{FeS}_2@\text{NC}$. $\text{FeSe}_2@\text{NC}$ was synthesized via similar procedure. Briefly, $\text{Fe}_3\text{O}_4@\text{NC}$ and excess Se powder were separately put into both ends of a porcelain boat and heated to 500 °C (2 °C min^{-1}) for 8 h under a mixed H_2/Ar flow with 10 vol% H_2 .

Material characterization. The morphology and structure of the samples were characterized by field emission scanning electron microscope (FESEM; HITACHI SU6600) and transmission electron microscope (TEM; JEOL; JEM-2100F). The crystal structures, valence states and total carbon content were investigated by X-ray diffraction (XRD; Bruker AXS D8 Advance), Raman

Spectrometer (Horiba JOBIN YVON; HR 800) and thermogravimetric analysis (TGA, Perkin-Elmer TGA 7), respectively. The X-ray photoelectron spectroscopy (XPS) spectrum was performed on ESCA Lab 250 (USA) with monochromatic Al K sources. The chemical bonds were analyzed by Micro-Infrared Spectroscopy (Bruker VERTEX70).

Electrochemical measurements. The electrochemical measurements of the half cell were carried out using CR2025 coin-type cells with a metallic potassium foil as the counter electrode, and 1 M potassium bis(fluorosulfonyl)imide (KFSI) in the diethyl carbonate/ethylene carbonate (DEC/EC, v/v, 1:1) as the electrolyte. Glass microfiber (Whatman GF/D) was used as the separator. The electrodes were prepared by mixing the active material with sodium carboxymethyl cellulose (CMC) and conductive agent (Super-P-Li) in a weight ratio of 7:2:1 using deionized water as a solvent. The resultant slurry was coated on an Al foil and dried in a vacuum oven at 60 °C for 12 h. The full cell was assembled using reduced graphene oxide supported polyimide composite (PI@rGO) as the cathode. (See the Supporting Information for the preparation methods of PI@rGO) The mass ratio of anode and cathode was about 1:2. Both the cathode and the anode underwent several cycles of activation in a half cell before being assembled into a full cell. The voltage window of the full battery is 0.1-3 V. The cell was assembled in an Ar-filled glovebox (Dellix, [O₂] < 0.1 ppm, [H₂O] < 0.1 ppm).

ASSOCIATED CONTENT

Supporting Information

The Supporting Information is available free of charge on the ACS Publications website at DOI:

Additional experimental methods, FESEM images, EDX, XPS spectra, electrochemical characterizations, DOS, TEM images, supplementary discussion and tables.

AUTHOR INFORMATION

Corresponding Author

*E-mail: kx210@cam.ac.uk. (K. Xi)

*E-mail: gaoguoxin@mail.xjtu.edu.cn. (G. Gao)

*E-mail: dingsj@xjtu.edu.cn (S. Ding)

*E-mail: yguo@whu.edu.cn (Y. Guo)

Author Contributions

[†]H. Wu, S. Lu, and S. Xu contributed equally to this work. S. Lu, H. Wu, K. Xi, and G. Gao conceived and designed this work; S. Lu, H. Wu, S. Xu, Y. Wang, J. Zhao and C. Huang performed the experiments, characterizations, calculations and simulations; H. Wu, S. Lu and K. Xi wrote the manuscript; H. Wu, S. Lu, K. Xi, A. Abdelkader, G. Gao, S. Ding, W. Wang, Y. Guo and R. V. Kumar analyzed the data and revised the manuscript. All authors have given approval to the final version of the manuscript.

Notes

The authors declare no competing financial interest.

ACKNOWLEDGEMENT

This research was supported by the National Natural Science Foundation of China (No. 51773165, 51973171), Natural Science Foundation of Shaanxi Province (No. 2019JM-175), Key Laboratory Construction Program of Xi'an Municipal Bureau of Science and Technology (201805056ZD7CG40). The numerical calculations in this paper have been done on the supercomputing system in the Supercomputing Center of Wuhan University. The authors would like to thank the Center for Advancing Materials Performance from the Nanoscale (CAMP-Nano) for allowing the use of field-emission scanning electron microscopy. We also thank Mr. Chang

Huang at Instrument Analysis Center of Xi'an Jiaotong University for their assistance with XRD analysis.

REFERENCES

1. Dunn, B.; Kamath, H.; Tarascon, J.-M. J. S. Electrical Energy Storage for the Grid: A Battery of Choices. *Science* **2011**, *334*, 928-935.
2. Yabuuchi, N.; Kubota, K.; Dahbi, M.; Komaba, S. Research Development on Sodium-Ion Batteries. *Chem. Rev.* **2014**, *114*, 11636-82.
3. Kubota, K.; Dahbi, M.; Hosaka, T.; Kumakura, S.; Komaba, S. Towards K-Ion and Na-Ion Batteries as “Beyond Li-Ion”. *Chem. Rec.* **2018**, *18*, 459-479.
4. Zhang, W.; Liu, Y.; Guo, Z. Approaching High-Performance Potassium-Ion Batteries via Advanced Design Strategies and Engineering. *Sci. Adv.* **2019**, *5*, eaav7412.
5. Hwang, J. Y.; Myung, S. T.; Sun, Y. K. Sodium-Ion Batteries: Present and Future. *Chem. Soc. Rev.* **2017**, *46*, 3529-3614.
6. Zhang, W.; Pang, W. K.; Sencadas, V.; Guo, Z. Understanding High-Energy-Density Sn₄P₃ Anodes for Potassium-Ion Batteries. *Joule* **2018**, *2*, 1534-1547.
7. Zhang, W.; Mao, J.; Li, S.; Chen, Z.; Guo, Z. Phosphorus-Based Alloy Materials for Advanced Potassium-Ion Battery Anode. *J. Am. Chem. Soc.* **2017**, *139*, 3316-3319.
8. Tan, H.; Feng, Y.; Rui, X.; Yu, Y.; Huang, S. Metal Chalcogenides: Paving the Way for High-Performance Sodium/Potassium-Ion Batteries. *Small Methods* **2019**, *4*, 1900563.
9. Zhao, J.; Zou, X.; Zhu, Y.; Xu, Y.; Wang, C. Electrochemical Intercalation of Potassium into Graphite. *Adv. Funct. Mater.* **2016**, *26*, 8103-8110.
10. Ding, J.; Zhang, H.; Zhou, H.; Feng, J.; Zheng, X.; Zhong, C.; Paek, E.; Hu, W.; Mitlin, D. Sulfur-Grafted Hollow Carbon Spheres for Potassium-Ion Battery Anodes. *Adv. Mater.* **2019**, *31*, 1900429.
11. Liu, Z.; Wang, J.; Jia, X.; Li, W.; Zhang, Q.; Fan, L.; Ding, H.; Yang, H.; Yu, X.; Li, X.; Lu, B. Graphene Armored with a Crystal Carbon Shell for Ultrahigh-Performance Potassium Ion Batteries and Aluminum Batteries. *ACS Nano* **2019**, *13*, 10631-10642.
12. Li, Y.; Yang, C.; Zheng, F.; Pan, Q.; Liu, Y.; Wang, G.; Liu, T.; Hu, J.; Liu, M. Design of TiO₂eC Hierarchical Tubular Heterostructures for High Performance Potassium Ion Batteries.

Nano Energy **2019**, *59*, 582-590.

13. Wang, N.; Chu, C.; Xu, X.; Du, Y.; Yang, J.; Bai, Z.; Dou, S. Comprehensive New Insights and Perspectives into Ti-Based Anodes for Next-Generation Alkaline Metal (Na⁺, K⁺) Ion Batteries. *Adv. Energy Mater.* **2018**, *8*, 1801888.
14. Huang, H.; Cui, J.; Liu, G.; Bi, R.; Zhang, L. Carbon-Coated MoSe₂/MXene Hybrid Nanosheets for Superior Potassium Storage. *ACS Nano* **2019**, *13*, 3448-3456.
15. Bin, D.-S.; Duan, S.-Y.; Lin, X.-J.; Liu, L.; Liu, Y.; Xu, Y.-S.; Sun, Y.-G.; Tao, X.-S.; Cao, A.-M.; Wan, L.-J. Structural Engineering of SnS₂/Graphene Nanocomposite for High-Performance K-Ion Battery Anode. *Nano Energy* **2019**, *60*, 912-918.
16. Chong, S.; Wu, Y.; Liu, C.; Chen, Y.; Guo, S.; Liu, Y.; Cao, G. Cryptomelane-Type MnO₂/Carbon Nanotube Hybrids as Bifunctional Electrode Material for High Capacity Potassium-Ion Full Batteries. *Nano Energy* **2018**, *54*, 106-115.
17. Dong, Y.; Xu, Y.; Li, W.; Fu, Q.; Wu, M.; Manske, E.; Kroger, J.; Lei, Y. Insights into the Crystallinity of Layer-Structured Transition Metal Dichalcogenides on Potassium Ion Battery Performance: A Case Study of Molybdenum Disulfide. *Small* **2019**, *15*, 1900497.
18. Yang, C.; Feng, J.; Lv, F.; Zhou, J.; Lin, C.; Wang, K.; Zhang, Y.; Yang, Y.; Wang, W.; Li, J.; Guo, S. Metallic Graphene-Like VSe₂ Ultrathin Nanosheets: Superior Potassium-Ion Storage and Their Working Mechanism. *Adv. Mater.* **2018**, *30*, 1800036.
19. Wu, Y.; Hu, S.; Xu, R.; Wang, J.; Peng, Z.; Zhang, Q.; Yu, Y. Boosting Potassium-Ion Battery Performance by Encapsulating Red Phosphorus in Free-Standing Nitrogen-Doped Porous Hollow Carbon Nanofibers. *Nano Lett.* **2019**, *19*, 1351-1358.
20. Zhang, Q.; Mao, J.; Pang, W. K.; Zheng, T.; Sencadas, V.; Chen, Y.; Liu, Y.; Guo, Z. Boosting the Potassium Storage Performance of Alloy-Based Anode Materials via Electrolyte Salt Chemistry. *Adv. Energy Mater.* **2018**, *8*, 1703288.
21. Zheng, J.; Yang, Y.; Fan, X.; Ji, G.; Ji, X.; Wang, H.; Hou, S.; Zachariah, M. R.; Wang, C. Extremely Stable Antimony–Carbon Composite Anodes for Potassium-Ion Batteries. *Energy Environ. Sci.* **2019**, *12*, 615-623.
22. Lu, S.; Wu, H.; Hou, J.; Liu, L.; Li, J.; Harris, C. J.; Lao, C.-Y.; Guo, Y.; Xi, K.; Ding, S.; Gao, G.; Cheetham, A. K.; Kumar, R. V. Phase Boundary Engineering of Metal-Organic-Framework-Derived Carbonaceous Nickel Selenides for Sodium-Ion Batteries. *Nano Research* **2020**, DOI: 10.1007/s12274-020-2848-z.
23. Lu, S.; Zhu, T.; Wu, H.; Wang, Y.; Li, J.; Abdelkader, A.; Xi, K.; Wang, W.; Li, Y.; Ding, S.;

- Gao, G.; Kumar, R. V. Construction of Ultrafine ZnSe Nanoparticles On/In Amorphous Carbon Hollow Nanospheres with High-Power-Density Sodium Storage. *Nano Energy* **2019**, *59*, 762-772.
24. Fang, L.; Xu, J.; Sun, S.; Lin, B.; Guo, Q.; Luo, D.; Xia, H. Few-Layered Tin Sulfide Nanosheets Supported on Reduced Graphene Oxide as a High-Performance Anode for Potassium-Ion Batteries. *Small* **2019**, *15*, 1804806.
 25. Kaneti, Y. V.; Tang, J.; Salunkhe, R. R.; Jiang, X.; Yu, A.; Wu, K. C.; Yamauchi, Y. Nanoarchitected Design of Porous Materials and Nanocomposites from Metal-Organic Frameworks. *Adv. Mater.* **2017**, *29*, 1604898.
 26. Zhu, Y.; Fan, X.; Suo, L.; Luo, C.; Gao, T.; Wang, C. Electrospun FeS₂@Carbon Fiber Electrode as a High Energy Density Cathode for Rechargeable Lithium Batteries. *ACS Nano* **2016**, *10*, 1529-38.
 27. Chen, W.; Qi, S.; Guan, L.; Liu, C.; Cui, S.; Shen, C.; Mi, L. Pyrite FeS₂ Microspheres Anchoring on Reduced Graphene Oxide Aerogel as an Enhanced Electrode Material for Sodium-Ion Batteries. *J. Mater. Chem. A* **2017**, *5*, 5332-5341.
 28. Chen, K.; Zhang, W.; Xue, L.; Chen, W.; Xiang, X.; Wan, M.; Huang, Y. Mechanism of Capacity Fade in Sodium Storage and the Strategies of Improvement for FeS₂ Anode. *ACS Appl. Mater. Interfaces* **2017**, *9*, 1536-1541.
 29. Xi, K.; He, D.; Harris, C.; Wang, Y.; Lai, C.; Li, H.; Coxon, P. R.; Ding, S.; Wang, C.; Kumar, R. V. Enhanced Sulfur Transformation by Multifunctional FeS₂/FeS/S Composites for High-Volumetric Capacity Cathodes in Lithium-Sulfur Batteries. *Adv. Sci.* **2019**, *6*, 1800815.
 30. Zhao, Z.; Hu, Z.; Jiao, R.; Tang, Z.; Dong, P.; Li, Y.; Li, S.; Li, H. Tailoring Multi-Layer Architected FeS₂@C Hybrids for Superior Sodium-, Potassium- and Aluminum-Ion Storage. *Energy Storage Mater.* **2019**, *22*, 228-234.
 31. Chen, C.; Yang, Y.; Tang, X.; Qiu, R.; Wang, S.; Cao, G.; Zhang, M. Graphene-Encapsulated FeS₂ in Carbon Fibers as High Reversible Anodes for Na⁺/K⁺ Batteries in a Wide Temperature Range. *Small* **2019**, *15*, 1804740.
 32. Han, K.; Liu, Z.; Li, P.; Yu, Q.; Wang, W.; Lao, C.-Y.; He, D.; Zhao, W.; Suo, G.; Guo, H.; Song, L.; Qin, M.; Qu, X. High-throughput Fabrication of 3D N-Doped Graphenic Framework Coupled with Fe₃C@Porous Graphite Carbon for Ultrastable Potassium Ion Storage. *Energy Storage Mater.* **2019**, *22*, 185-193.
 33. Tan, Q.; Li, P.; Han, K.; Liu, Z.; Li, Y.; Zhao, W.; He, D.; An, F.; Qin, M.; Qu, X. Chemically

- Bubbled Hollow Fe_xO Nanospheres Anchored on 3D N-Doped Few-Layer Graphene Architecture as a Performance-Enhanced Anode Material for Potassium-Ion Batteries. *J. Mater. Chem. A* **2019**, *7*, 744-754.
34. Yang, F.; Gao, H.; Hao, J.; Zhang, S.; Li, P.; Liu, Y.; Chen, J.; Guo, Z. Yolk–Shell Structured $\text{FeP}@C$ Nanoboxes as Advanced Anode Materials for Rechargeable Lithium-/Potassium-Ion Batteries. *Adv. Funct. Mater.* **2019**, *29*, 1808291.
 35. Zhao, Y.; Zhu, J.; Ong, S. J. H.; Yao, Q.; Shi, X.; Hou, K.; Xu, Z. J.; Guan, L. High-Rate and Ultralong Cycle-Life Potassium Ion Batteries Enabled by In Situ Engineering of Yolk-Shell $\text{FeS}_2@C$ Structure on Graphene Matrix. *Adv. Energy Mater.* **2018**, *8*, 1802565.
 36. Zhao, W.; Guo, C.; Li, C. M. Lychee-Like $\text{FeS}_2@FeSe_2$ Core–Shell Microspheres Anode in Sodium Ion Batteries for Large Capacity and Ultralong Cycle Life. *J. Mater. Chem. A* **2017**, *5*, 19195-19202.
 37. Chen, M.; Liu, Q.; Wang, S. W.; Wang, E.; Guo, X.; Chou, S. L. High-Abundance and Low-Cost Metal-Based Cathode Materials for Sodium-Ion Batteries: Problems, Progress, and Key Technologies. *Adv. Energy Mater.* **2019**, *9*, 1803609.
 38. Lu, Z.; Zhai, Y.; Wang, N.; Zhang, Y.; Xue, P.; Guo, M.; Tang, B.; Huang, D.; Wang, W.; Bai, Z.; Dou, S. FeS_2 Nanoparticles Embedded in N/S Co-Doped Porous Carbon Fibers as Anode for Sodium-Ion Batteries. *Chem. Eng. J.* **2020**, *380*, 122455.
 39. Ge, P.; Zhang, C.; Hou, H.; Wu, B.; Zhou, L.; Li, S.; Wu, T.; Hu, J.; Mai, L.; Ji, X. Anions Induced Evolution of Co_3X_4 ($\text{X} = \text{O}, \text{S}, \text{Se}$) as Sodium-Ion Anodes: The Influences of Electronic Structure, Morphology, Electrochemical Property. *Nano Energy* **2018**, *48*, 617-629.
 40. Wang, D.; Zhou, W.; Zhang, R.; Zeng, J.; Du, Y.; Qi, S.; Cong, C.; Ding, C.; Huang, X.; Wen, G.; Yu, T. Mass Production of Large-Sized, Nonlayered 2D Nanosheets: Their Directed Synthesis by a Rapid "Gel-Blowing" Strategy, and Applications in Li/Na Storage and Catalysis. *Adv. Mater.* **2018**, *30*, 1803569.
 41. Uhlig, I.; Szargan, R.; Nwsbitt, H. W.; Laajalehto, K. Surface States and Reactivity of Pyrite and Marcasite. *Appl. Surf. Sci.* **2001**, *179*, 222-229.
 42. Li, W.; Zhou, M.; Li, H.; Wang, K.; Cheng, S.; Jiang, K. A High Performance Sulfur-Doped Disordered Carbon Anode for Sodium Ion Batteries. *Energy Environ. Sci.* **2015**, *8*, 2916-2921.
 43. Wang, T.; Zhai, P.; Legut, D.; Wang, L.; Liu, X.; Li, B.; Dong, C.; Fan, Y.; Gong, Y.; Zhang,

- Q. S-Doped Graphene-Regional Nucleation Mechanism for Dendrite-Free Lithium Metal Anodes. *Adv. Energy Mater.* **2019**, *9*, 1804000.
44. Xu, Y.; Zhang, C.; Zhou, M.; Fu, Q.; Zhao, C.; Wu, M.; Lei, Y. Highly Nitrogen Doped Carbon Nanofibers with Superior Rate Capability and Cyclability for Potassium Ion Batteries. *Nat. Commun.* **2018**, *9*, 1720.
45. Gao, X.; Wang, B.; Zhang, Y.; Liu, H.; Liu, H.; Wu, H.; Dou, S. Graphene-Scroll-Sheathed α -MnS Coaxial Nanocables Embedded in N, S Co-Doped Graphene Foam as 3D Hierarchically Ordered Electrodes for Enhanced Lithium Storage. *Energy Storage Mater.* **2019**, *16*, 46-55.
46. Liu, Y.; Qiao, Y.; Wei, G.; Li, S.; Lu, Z.; Wang, X.; Lou, X. Sodium Storage Mechanism of N, S Co-Doped Nanoporous Carbon: Experimental Design and Theoretical Evaluation. *Energy Storage Mater.* **2018**, *11*, 274-281.
47. He, H.; Huang, D.; Gan, Q.; Hao, J.; Liu, S.; Wu, Z.; Pang, W. K.; Johannessen, B.; Tang, Y.; Luo, J. L.; Wang, H.; Guo, Z. Anion Vacancies Regulating Endows MoSSe with Fast and Stable Potassium Ion Storage. *ACS Nano* **2019**, *13*, 11843-11852.
48. Han, Y.; Li, T.; Li, Y.; Tian, J.; Yi, Z.; Lin, N.; Qian, Y. Stabilizing Antimony Nanocrystals within Ultrathin Carbon Nanosheets for High-Performance K-Ion Storage. *Energy Storage Mater.* **2019**, *20*, 46-54.
49. Wang, J.; Fan, L.; Liu, Z.; Chen, S.; Zhang, Q.; Wang, L.; Yang, H.; Yu, X.; Lu, B. In Situ Alloying Strategy for Exceptional Potassium Ion Batteries. *ACS Nano* **2019**, *13*, 3703-3713.
50. Li, L.; Zhang, W.; Wang, X.; Zhang, S.; Liu, Y.; Li, M.; Zhu, G.; Zheng, Y.; Zhang, Q.; Zhou, T.; Pang, W. K.; Luo, W.; Guo, Z.; Yang, J. Hollow-Carbon-Templated Few-Layered V_5S_8 Nanosheets Enabling Ultrafast Potassium Storage and Long-Term Cycling. *ACS Nano* **2019**, *13*, 7939-7948.
51. Ge, J.; Fan, L.; Wang, J.; Zhang, Q.; Liu, Z.; Zhang, E.; Liu, Q.; Yu, X.; Lu, B. MoSe₂/N-Doped Carbon as Anodes for Potassium-Ion Batteries. *Adv. Energy Mater.* **2018**, *8*, 1801477.
52. Chen, M.; Wang, W.; Liang, X.; Gong, S.; Liu, J.; Wang, Q.; Guo, S.; Yang, H. Sulfur/Oxygen Codoped Porous Hard Carbon Microspheres for High-Performance Potassium-Ion Batteries. *Adv. Energy Mater.* **2018**, *8*, 1800171.
53. Wu, H.; Yu, Q.; Lao, C.-Y.; Qin, M.; Wang, W.; Liu, Z.; Man, C.; Wang, L.; Jia, B.; Qu, X. Scalable Synthesis of VN Quantum Dots Encapsulated in Ultralarge Pillared N-Doped Mesoporous Carbon Microsheets for Superior Potassium Storage. *Energy Storage Mater.* **2019**, *18*, 43-50.

54. Wang, W.; Jiang, B.; Qian, C.; Lv, F.; Feng, J.; Zhou, J.; Wang, K.; Yang, C.; Yang, Y.; Guo, S. Pistachio-Shuck-Like MoSe₂/C Core/Shell Nanostructures for High-Performance Potassium-Ion Storage. *Adv. Mater.* **2018**, *30*, 1801812.
55. Yu, Q.; Jiang, B.; Hu, J.; Lao, C. Y.; Gao, Y.; Li, P.; Liu, Z.; Suo, G.; He, D.; Wang, W. A.; Yin, G. Metallic Octahedral CoSe₂ Threaded by N-Doped Carbon Nanotubes: A Flexible Framework for High-Performance Potassium-Ion Batteries. *Adv. Sci.* **2018**, *5*, 1800782.
56. Cui, Y.; Liu, W.; Feng, W.; Zhang, Y.; Du, Y.; Liu, S.; Wang, H.; Chen, M.; Zhou, J. Controlled Design of Well-Dispersed Ultrathin MoS₂ Nanosheets inside Hollow Carbon Skeleton: Toward Fast Potassium Storage by Constructing Spacious “Houses” for K Ions. *Adv. Funct. Mater.* **2020**, *30*, 1908755.
57. Ruan, J.; Zhao, Y.; Luo, S.; Yuan, T.; Yang, J.; Sun, D.; Zheng, S. Fast and Stable Potassium-Ion Storage Achieved by In Situ Molecular Self-Assembling N/O Dual-Doped Carbon Network. *Energy Storage Mater.* **2019**, *23*, 46-54.
58. Yang, C.; Lv, F.; Zhang, Y.; Wen, J.; Dong, K.; Su, H.; Lai, F.; Qian, G.; Wang, W.; Hilger, A.; Xu, Y.; Zhu, Y.; Deng, Y.; Hu, W.; Manke, I.; Chen, Y. Confined Fe₂VO₄⊂Nitrogen-Doped Carbon Nanowires with Internal Void Space for High-Rate and Ultrastable Potassium-Ion Storage. *Adv. Energy Mater.* **2019**, *9*, 1902674.
59. Li, P.; Wang, W.; Gong, S.; Lv, F.; Huang, H.; Luo, M.; Yang, Y.; Yang, C.; Zhou, J.; Qian, C.; Wang, B.; Wang, Q.; Guo, S. Hydrogenated Na₂Ti₃O₇ Epitaxially Grown on Flexible N-Doped Carbon Sponge for Potassium-Ion Batteries. *ACS Appl. Mater. Interfaces* **2018**, *10*, 37974-37980.
60. An, Y.; Tian, Y.; Ci, L.; Xiong, S.; Feng, J.; Qian, Y. Micron-Sized Nanoporous Antimony with Tunable Porosity for High-Performance Potassium-Ion Batteries. *ACS Nano* **2018**, *12*, 12932-12940.
61. Lin, H.; Li, M.; Yang, X.; Yu, D.; Zeng, Y.; Wang, C.; Chen, G.; Du, F. Nanosheets-Assembled CuSe Crystal Pillar as a Stable and High-Power Anode for Sodium-Ion and Potassium-Ion Batteries. *Adv. Energy Mater.* **2019**, *9*, 1900323.
62. Xu, X.; Liu, J.; Liu, J.; Ouyang, L.; Hu, R.; Wang, H.; Yang, L.; Zhu, M. A General Metal-Organic Framework (MOF)-Derived Selenidation Strategy for In Situ Carbon-Encapsulated Metal Selenides as High-Rate Anodes for Na-Ion Batteries. *Adv. Funct. Mater.* **2018**, *28*, 1707573.
63. Ge, P.; Hou, H.; Li, S.; Yang, L.; Ji, X. Tailoring Rod-Like FeSe₂ Coated with Nitrogen-

Doped Carbon for High-Performance Sodium Storage. *Adv. Funct. Mater.* **2018**, *28*, 1801765.

64. Fang, G.; Wang, Q.; Zhou, J.; Lei, Y.; Chen, Z.; Wang, Z.; Pan, A.; Liang, S. Metal Organic Framework-Templated Synthesis of Bimetallic Selenides with Rich Phase Boundaries for Sodium-Ion Storage and Oxygen Evolution Reaction. *ACS Nano* **2019**, *13*, 5635-5645.
65. Tang, Y.; Zhao, Z.; Hao, X.; Wei, Y.; Zhang, H.; Dong, Y.; Wang, Y.; Pan, X.; Hou, Y.; Wang, X.; Qiu, J. Cellular Carbon-Wrapped FeSe₂ Nanocavities with Ultrathin Walls and Multiple Rooms for Ion Diffusion-Confined Ultrafast Sodium Storage. *J. Mater. Chem. A* **2019**, *7*, 4469-4479.
66. Jain, A.; Ong, S. P.; Hautier, G.; Chen, W.; Richards, W. D.; Dacek, S.; Cholia, S.; Gunter, D.; Skinner, D.; Ceder, G.; Persson, K. A. Commentary: The Materials Project: A Materials Genome Approach to Accelerating Materials Innovation. *APL Mater.* **2013**, *1*, 011002.
67. Yu, S.; Hong Ng, V. M.; Wang, F.; Xiao, Z.; Li, C.; Kong, L. B.; Que, W.; Zhou, K. Synthesis and Application of Iron-Based Nanomaterials as Anodes of Lithium-Ion Batteries and Supercapacitors. *J. Mater. Chem. A* **2018**, *6*, 9332-9367.

Figures

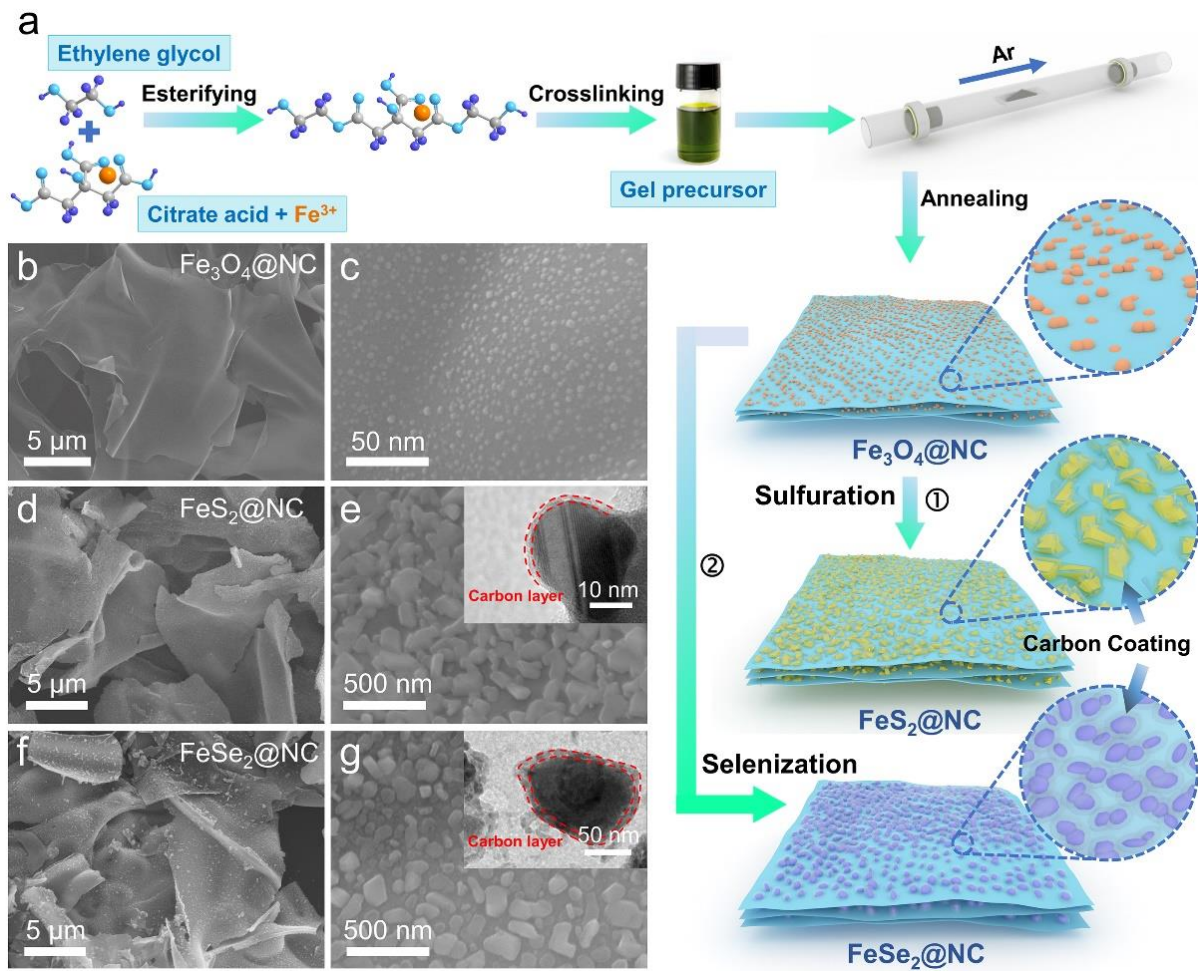


Figure 1. (a) Schematic illustration for the synthesis of Fe₃O₄@NC, FeS₂@NC and FeSe₂@NC. FESEM images of (b, c) Fe₃O₄@NC, (d, e) FeS₂@NC and (f, g) FeSe₂@NC. The insets in (e) and (g) are HRTEM images, showing the Fe-based particles are coated by amorphous carbon.

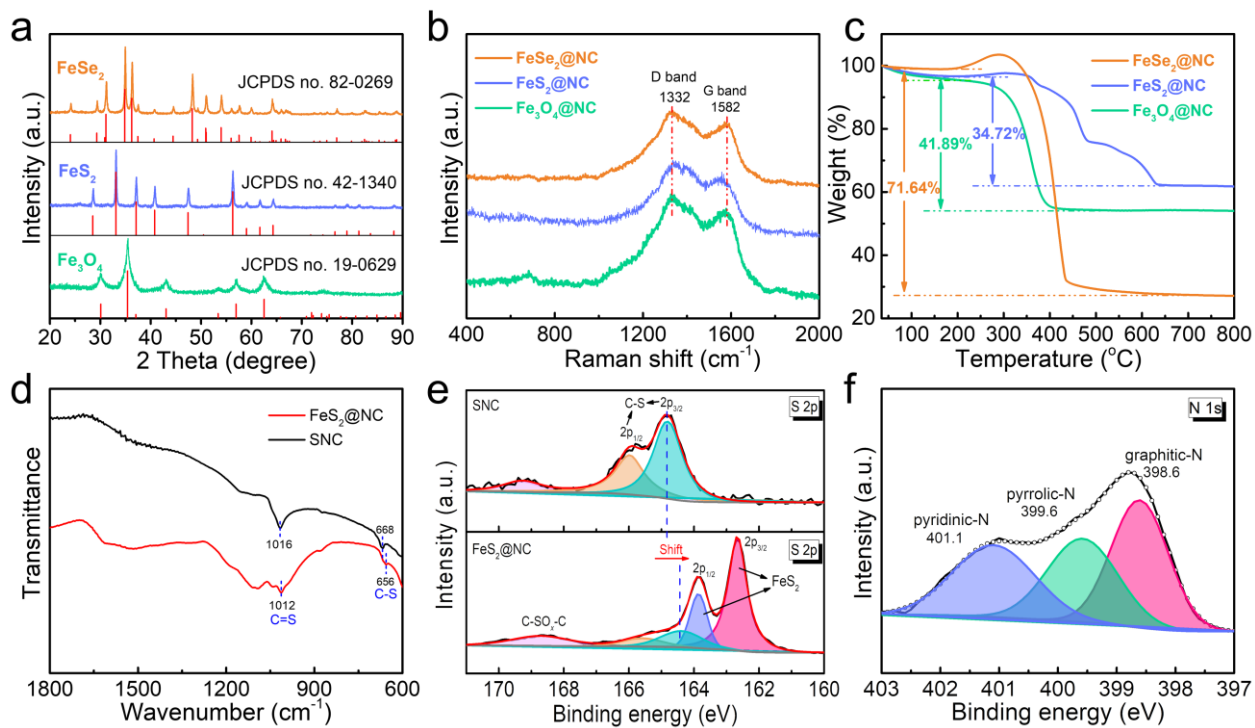


Figure 2. (a) XRD patterns, (b) Raman spectra, and (c) TGA curves of $\text{Fe}_3\text{O}_4@\text{NC}$, $\text{FeS}_2@\text{NC}$ and $\text{FeSe}_2@\text{NC}$. (d) FT-IR and (e) high-resolution S 2p XPS spectra of $\text{FeS}_2@\text{NC}$ and SNC. (f) N 1s XPS spectra of $\text{FeS}_2@\text{NC}$.

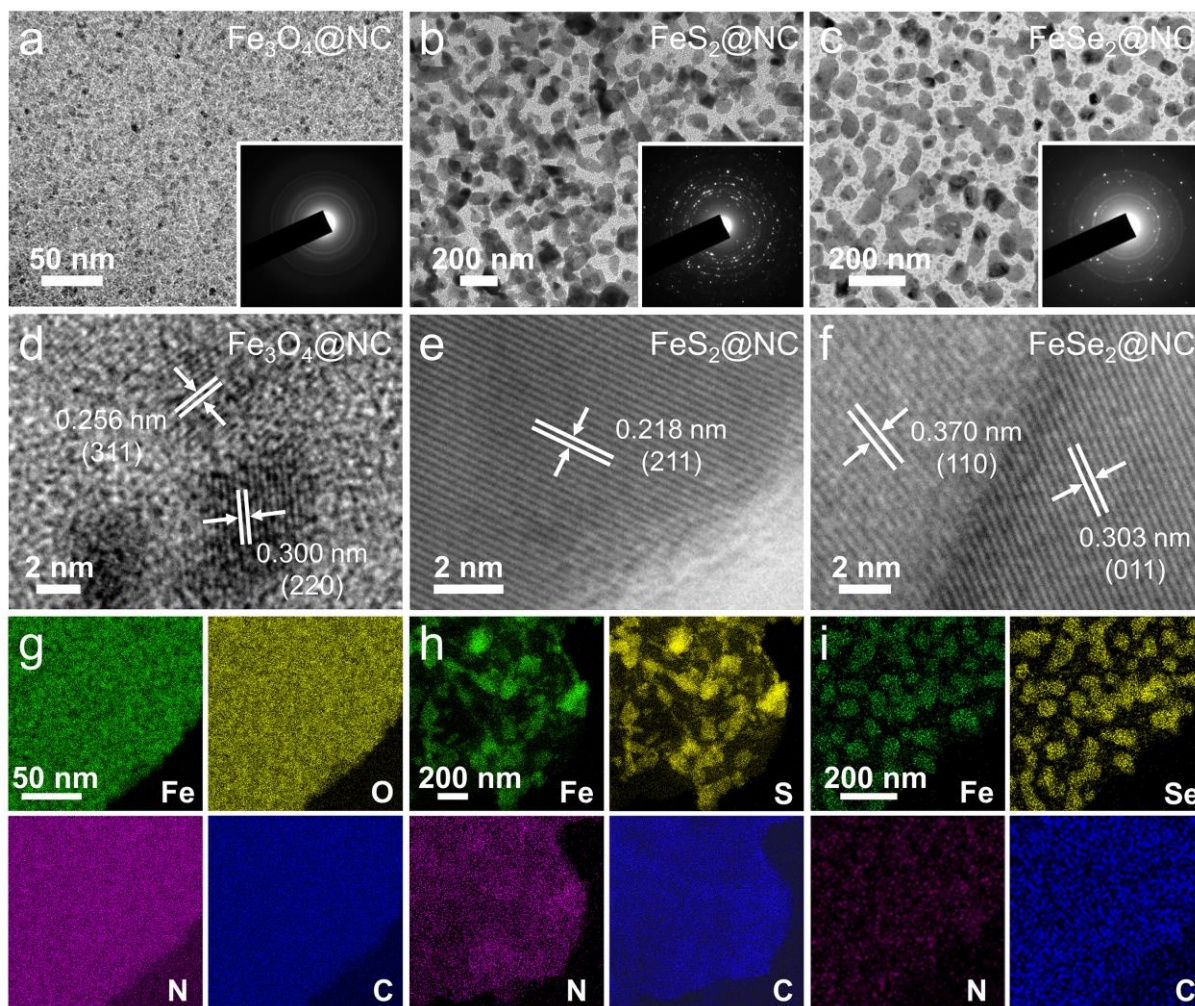


Figure 3. TEM, HRTEM images and elemental mapping of (a, d, g) Fe₃O₄@NC, (b, e, h) FeS₂@NC and (c, f, i) FeSe₂@NC, respectively. The insets of (a-c) are the corresponding SAED patterns.

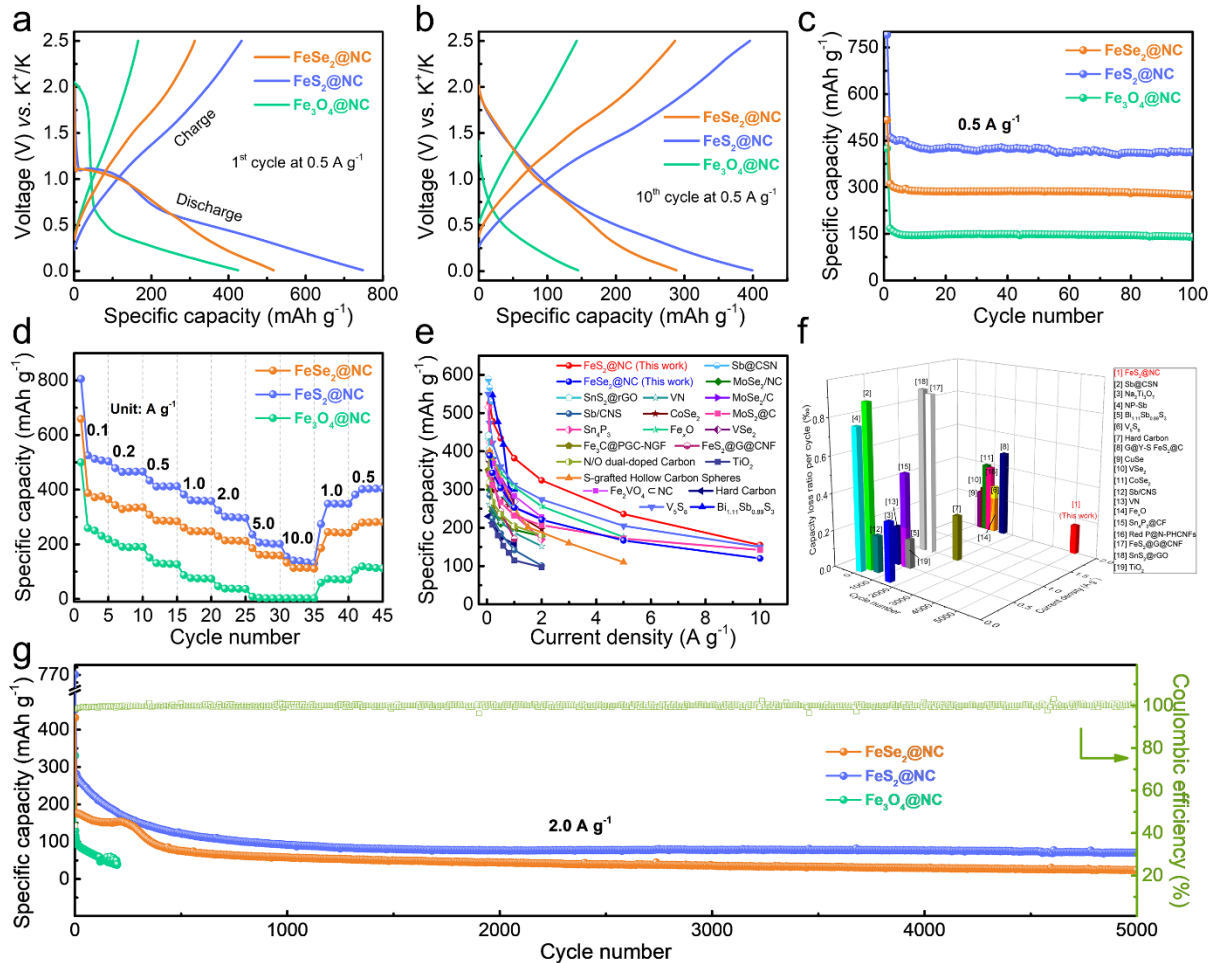


Figure 4. Electrochemical performance of Fe₃O₄@NC, FeS₂@NC and FeSe₂@NC anodes in PIBs: (a, b) charge-discharge profiles at 0.5 A g⁻¹ for the 1st cycle (a) and the 10th cycle (b); (c) cycling performance at 0.5 A g⁻¹; (d) rate capability at various current densities ranging from 0.1 to 10 A g⁻¹; Comparison of the (e) rate performance and (f) long-term cycle stability of FeS₂@NC in this work with other representative materials reported previously; (g) Long-term cycling performance and Coulombic efficiency at 2 A g⁻¹.

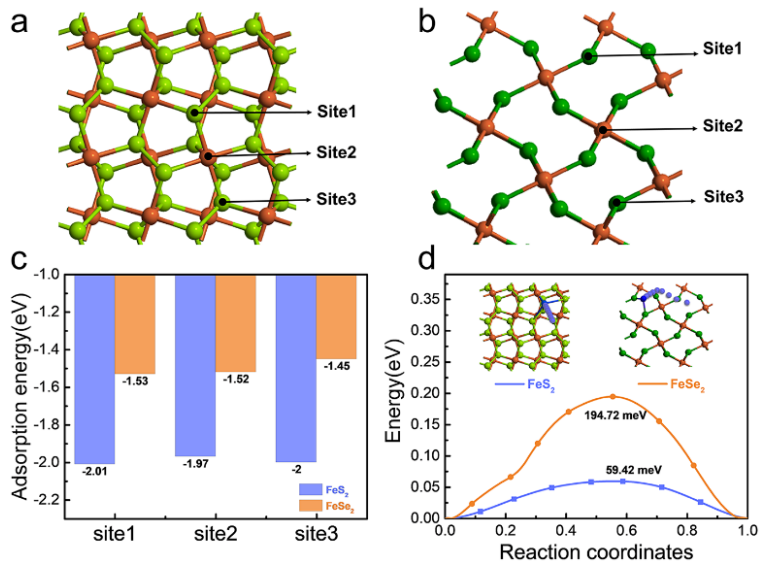


Figure 5. Different adsorption sites on (a) FeS₂ (001) and (b) FeSe₂ (110) surfaces. (c) The adsorption energy of K on two surfaces. (d) Diffusion energy barrier of K on FeS₂ and FeSe₂ surfaces. The insets in (d) show the diffusion process. (Fe: brown, S: light green, Se: dark green, K: blue)

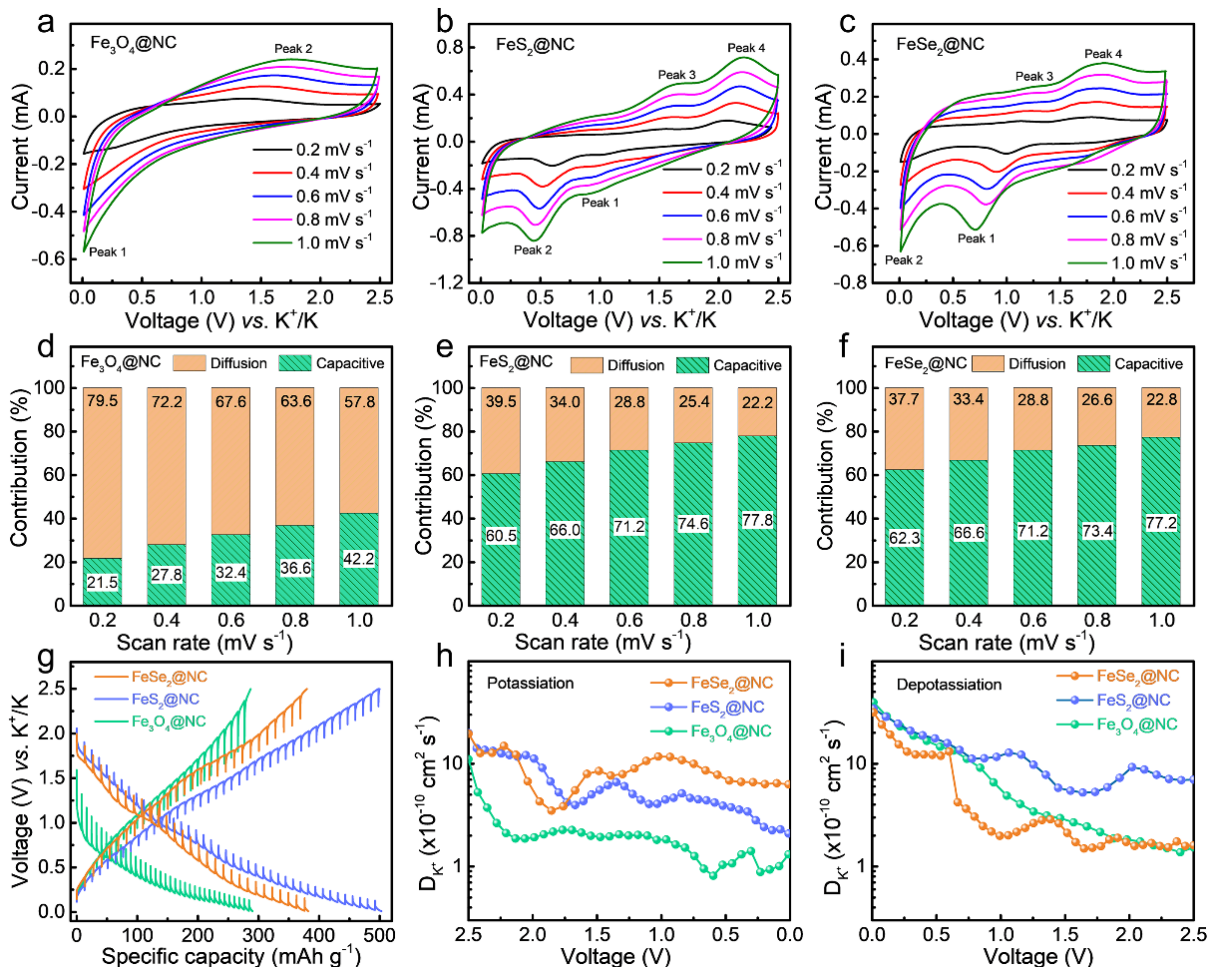


Figure 6. CV curves at different scan rates for (a) Fe₃O₄@NC, (b) FeS₂@NC and (c) FeSe₂@NC electrodes. Contribution ratio of the capacitive and diffusion–controlled capacities at different scan rates of (d) Fe₃O₄@NC, (e) FeS₂@NC and (f) FeSe₂@NC electrodes. (g) GITT profiles of the three samples. The diffusion coefficients of Fe₃O₄@NC, FeS₂@NC and FeSe₂@NC calculated from the GITT profiles as a function of potential for potassiation (h) and depotassiation processes (i).

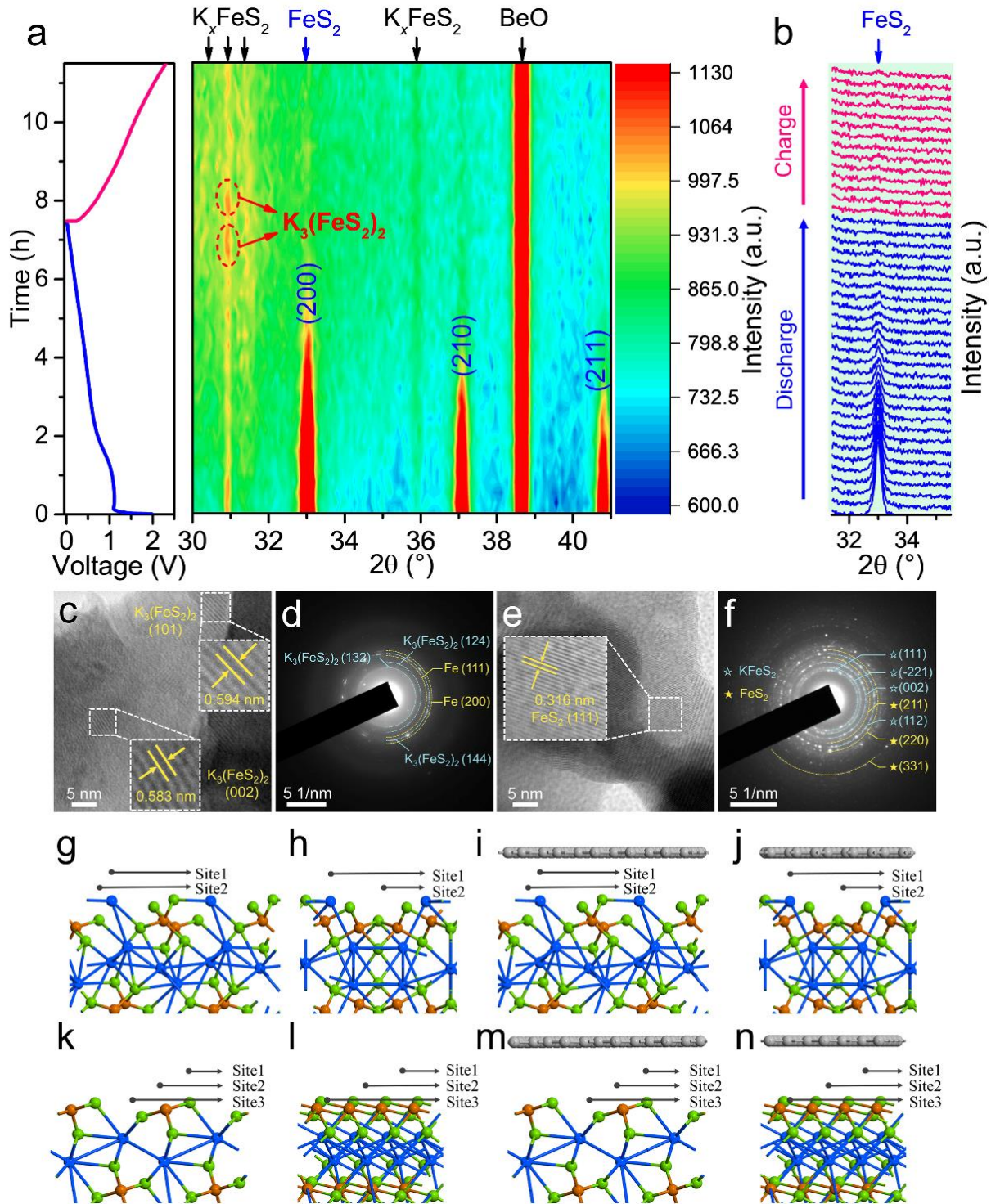


Figure 7. Potassium-ion storage mechanism study of FeS₂@NC anode: (a) *in-situ* XRD patterns collected during the first cycle and the corresponding discharge-charge profiles (on the left column). (b) Selected *in-situ* XRD patterns during the potassiation and depotassiation process. (c-

f) HRTEM images and the corresponding SAED patterns of FeS₂@NC after being discharged to 0.01 V (c, d) and after being charged to 2.5 V (e, f). (g) Front view and (h) side view of different adsorption sites on K₃(FeS₂)₂ (001) surface. (i) Front view and (j) side view of different adsorption sites on K₃(FeS₂)₂ (001) surface with graphene layer. (k) Front view and (l) side view of different adsorption sites on KFeS₂ (001) surface. (m) Front view and (n) side view of different adsorption sites on KFeS₂ (001) surface with graphene layer. (Fe: brown, S: green, K: blue)

Table 1. Adsorption energy of K on K₃(FeS₂)₂ (001) and KFeS₂ (001)

The adsorption position on two surfaces	K ₃ (FeS ₂) ₂		KFeS ₂		
	Site1	Site2	Site1	Site2	Site3
Adsorption energy with graphene (eV)	-2.46	-3.78	-2.99	-3.06	-3.01
Adsorption energy without graphene (eV)	-1.49	-2.15	-2.92	-2.93	-2.93

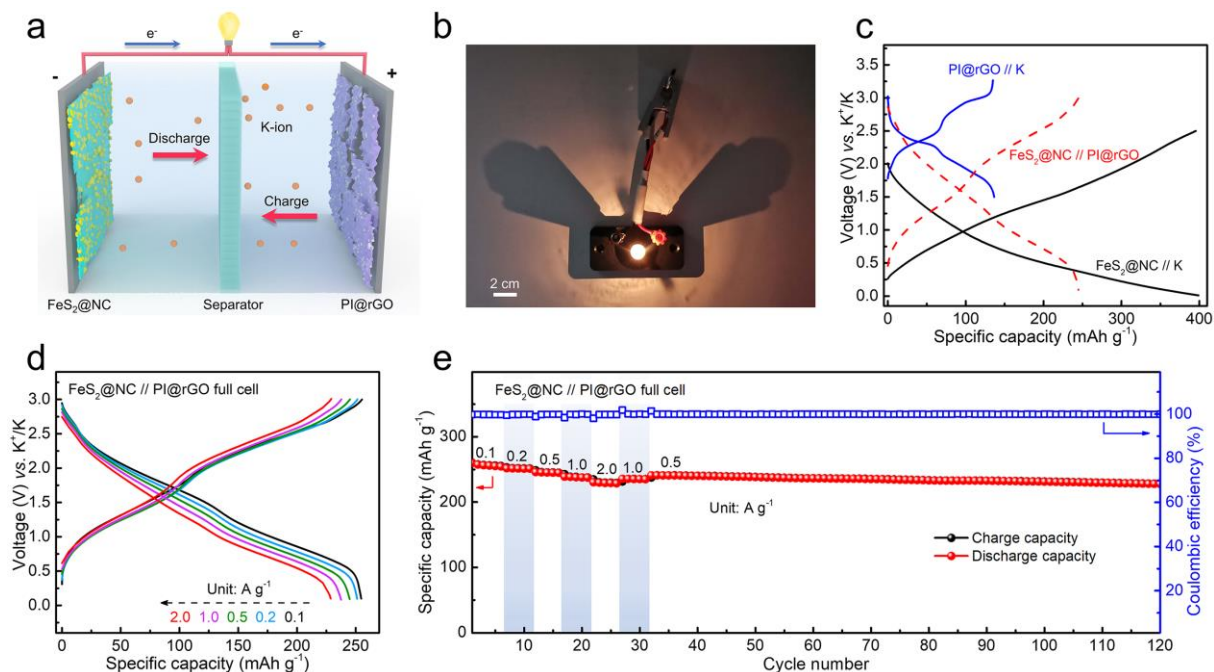


Figure 8. Electrochemical performance of the $\text{FeS}_2@\text{NC} // \text{PI}@r\text{GO}$ full cell for potassium storage: (a) Schematic illustration of the full cell. (b) The light bulb driven by the full cell. (c) Charge and discharge curves of $\text{FeS}_2@\text{NC} // \text{K}$ half cell, $\text{FeS}_2@\text{NC} // \text{PI}@r\text{GO}$ full cell and $\text{PI}@r\text{GO} // \text{K}$ half cell. (d) The charge and discharge curves at various current densities. (e) Rate and cycling performance.

For Table of Contents Use Only

Blowing Iron Chalcogenides into Two-Dimensional Flaky Hybrids with Superior Cyclability and Rate Capability for Potassium Ion Batteries 是不是加个全电池?

